Decoupled PQ Grid-Forming Control With Tunable Converter Frequency Behaviour

Citation for the original published paper (version of record):
Imgart, P., Narula, A., Bongiorno, M. et al (2026). Decoupled PQ Grid-Forming Control With Tunable Converter Frequency Behaviour. IEEE Open Journal of Industry Applications, 7: 148-162.
http://dx.doi.org/10.1109/OJIA.2026.3658761

IEEE Open Journal of
Industry Applications

Received 26 September 2025; revised 18 December 2025; accepted 23 January 2026. Date of publication 28 January 2026;
date of current version 6 February 2026.

Digital Object Identifier 10.1109/OJIA.2026.3658761

Decoupled PQ Grid-Forming Control With Tunable Converter Frequency Behavior

**PAUL IMGART [1] (Member, IEEE), ANANT NARULA [1] (Member, IEEE),
MASSIMO BONGIORNO [1] (Senior Member, IEEE), MEBTU BEZA [1] (Member, IEEE),
JAN R. SVENSSON [2] (Senior Member, IEEE), JEAN-PHILIPPE HASLER[3],
AND PAOLO MATTAVELLI [4] (Fellow, IEEE)**

[1]Department of Electrical Engineering, Chalmers University of Technology, 412 96 Göteborg, Sweden
[2]Hitachi Energy Research, 722 26 Vasteras, Sweden
[3]Hitachi Energy, Vasteras, 721 64 Vasteras, Sweden
[4]Department of Management and Engineering, University of Padova, 361 00 Vicenza, Italy

CORRESPONDING AUTHOR: ANANT NARULA (e-mail: anant.narula@chalmers.se)

ABSTRACT Grid-forming (GFM) converters are a widely-accepted solution for the challenges arising from the decarbonisation of electrical power systems. Ideally, a GFM converter should act as a slow-varying voltage source behind a (tunable) *RL* impedance to guarantee setpoint tracking and grid support. However, the inherent coupling between active and reactive power greatly limits the selection of the impedance's parameters often leading to the need for additional controllers, for example to provide damping at the synchronous-frequency resonance. This article proposes a decoupled power controller that combines a complex-power control loop with a virtual admittance to provide freely tunable parameters that provide damping at subsynchronous and synchronous frequency, decoupling of active and reactive power, as well as providing desired behavior over a wide range of frequency. The controller's performance is evaluated and compared to a conventional control approach both analytically and in a laboratory environment.

INDEX TERMS Frequency response, grid-forming (GFM) control, grid-forming inverters, power decoupling, virtual impedance.

NOMENCLATURE

List of symbols

S_{N}	Rated converter power.
V_{N}	Rated converter voltage.
ω_{N}	Rated angular frequency.
R_{g}	Grid resistance.
L_{g}	Grid inductance.
X_{g}	Grid reactance.
R_{f}	Filter resistance.
L_{f}	Filter inductance.
X_{f}	Filter reactance at rated frequency.
R_{v}	Virtual resistance.
L_{v}	Virtual inductance.
X_{v}	Virtual reactance at rated frequency.
$\underline{Y}_{\mathrm{v}}$	Virtual-admittance.
φ_{Y}	Virtual-admittance angle.
PCC	Point of common coupling.
v_{s}	Thévenin equivalent voltage source.
v_{g}	PCC voltage.
v_{c}	Converter's voltage.
v_{EMF}	Virtual-voltage source.
θ_{EMF}	Virtual voltage-source angle.
i_{f}	Filter current.
P_{g}	Exchanged active power.
Q_{g}	Exchanged reactive power.
δ	Angle difference between virtual-voltage source and PCC voltage.
H	Inertia time-constant.
α_{P}	Loop-bandwidth of active-power controller.
$K_{\mathrm{p,P}}$	Active-power controller proportional gain.
$K_{\mathrm{i,P}}$	Active-power controller integral gain.
$R_{\mathrm{a,P}}$	Active-damping term in active-power controller.
α_{Q}	Loop-bandwidth of reactive-power controller.
$K_{\mathrm{p,Q}}$	Reactive-power controller's proportional gain.
$K_{\mathrm{i,Q}}$	Reactive-power controller's integral gain.
$R_{\mathrm{a,Q}}$	Active-damping term in reactive-power controller.

γ	Output of active-power controller.
ε	Output of reactive-power controller.
$\underline{\kappa}$	Complex output of power controllers, $\gamma + j\varepsilon$.
$\underline{\xi}$	Phase-shifted complex output of power controllers.
ζ_P	Damping ratio of closed-loop active-power controller.
ζ_Q	Damping ratio of closed-loop reactive-power controller.
RoCoF	Rate of change of frequency.

I. INTRODUCTION

Global efforts to limit climate change through the reduction of greenhouse gas emissions result in an increase of electricity generation from renewable sources [1]. Together with other factors, such as increased utilization and flexibility of power grid assets as well as changing consumer technologies, the share of power electronics in electric power grids is rising [2]. Associated with this increase are concerns and challenges regarding the stability of converter-dominated power grids. Examples for these challenges are the decrease of mechanical inertia, reduced short-circuit current and risk for adverse control interaction [3].

A proposed solution to the challenges is the usage of grid-forming (GFM) converters, which are controlled as a slowly varying voltage source behind an impedance [3], [4]. A common feature in the large variety of GFM converter control designs available from the literature is that the active-power control determines the angle and reactive power determines the magnitude of the voltage source [5], [6], [7]. The assumption behind is a mainly inductive impedance between the controlled voltage and the grid connection, similar to a synchronous machine (SM). Among the most popular GFM control designs are the power-synchronization control [8] and the virtual admittance-based GFM control (VA-GFM) [9].

Despite their positive contribution to improving power system stability, GFM controllers face several challenges, including the following.

1) Coupling between active- and reactive-power dynamics [10], [11].
2) Insufficient damping of DC-current offsets [12].
3) Limited characterization and tunability of the converter input admittance in the subsynchronous and supersynchronous frequency ranges [12], [13].

These challenges can be addressed by decoupling the GFM's active- and reactive-power control loops and by proper selection of the parameters of the virtual impedance. Several solutions for GFM controllers aiming at decoupling the active-power loop (APL) and reactive-power loop (RPL) are available in the literature.One decoupling technique is based on virtual-impedance shaping, as the one introduced in [14], where a selective resistive virtual-impedance method is adopted. In the method, a tunable virtual resistance and a compensating virtual inductance are used to shape the small-signal impedance of the converter, resulting in an approximately resistive behavior in the low-frequency range ($0 - 20$ Hz in the rotating $dq-$frame). While this approach improves power decoupling, the selection of the virtual-impedance parameters is constrained by the loop bandwidths of the inner controllers. The use of a virtual-negative resistance to cancel the resistive component of the line impedance has been proposed in [15]. Although effective in achieving decoupling at the fundamental frequency, due to the introduction of a negative resistance this method may negatively impact the system's damping, especially in the subsynchronous frequency range.

Another class of decoupling techniques focuses on coordinate transformations and modified power definitions rather than impedance shaping. In [16] and [17], active and reactive powers are phase shifted by the angle of the steady-state impedance between the two voltage sources. However, the use of a steady-state representation of the impedance limits the effectiveness of this method to the fundamental frequency only. Furthermore, the proposed approach is not suitable for any arbitrary selection of the impedance parameters, for example when a virtual impedance is employed in the control strategy.

The authors in [18] and [19] proposed a preconditioning matrix within the control loop to eliminate the off-diagonal terms in the small-signal power-flow Jacobian. Although effective in decoupling power responses to set-point variations, the feedforward of reactive power into the APL—and vice versa, as in [19]—may compromise the desired voltage-source behavior of the converter during grid disturbances. Moreover, the dependence of the preconditioning matrix on the grid impedance angle in [18] might reduce the robustness of the decoupling performance under rapidly changing grid conditions.

More recently, an active-power feedforward scheme has been proposed in [20], where ideal decoupling voltages are computed based on the operating point of the converter. While this method enables decoupling over a wider frequency range, the additional voltage compensation term may reduce the converter's damping, especially at frequencies above the fundamental.

The aim of this article is to present a decoupled GFM converter controller based on the VA-GFM framework. The proposed controller achieves effective decoupling of active- and reactive-power dynamics over the frequency range in which the power controllers are active, while allowing independent and flexible selection of the virtual-admittance parameters to meet the desired frequency characteristic of the converter.

The rest of this article is organized as follows. Starting from the desired frequency characteristic of GFM converters, the basic operation of the VA-GFM control strategy together with the need for power decoupling is discussed in Section II. This is followed by a presentation of the proposed decoupled GFM controller in Section III and the controller's frequency characteristics in Section IV. Finally, the results from the experimental validation are discussed in Section V. Finally, Section VI concludes this article.

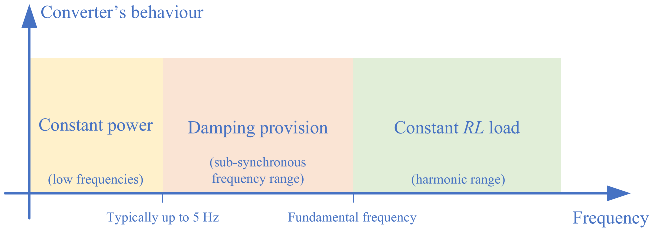

FIGURE 1. Desired behavior of GFM converters at different frequencies.

II. FREQUENCY CHARACTERIZATION OF GFM CONVERTERS AND THE NEED FOR POWER DECOUPLING

A. FREQUENCY CHARACTERIZATION

GFM control can be implemented in various forms, and a unified control structure still does not exist and remains an active topic of discussion in both industrial and academic communities [21]. Despite this diversity, a widely accepted characteristic of converter-interfaced resources employing GFM control is their ability to exhibit an internal-voltage phasor that remains constant—or nearly so—during the subtransient to transient time frames [3].

This behavior enables an almost instantaneous change in the converter-current phasor in response to grid disturbances, allowing converter-interfaced resources to provide immediate and natural support to the grid during contingencies. This dynamic performance is clearly superior to the more traditional grid-following (GFL) control, making GFM highly attractive for system operators [22].

Beyond the subtransient and transient time frames, the internal-voltage phasor must be controlled to maintain synchronism with the grid and to regulate both active- and reactive-power flows according to the predefined setpoints.

Consistent with the dynamic behavior outlined above, GFM converters are expected to exhibit a slowly varying voltage-source behavior behind a series impedance. The "slowness" in response is governed by the speed of the converter's power-control loops [22]. Furthermore, the control system should be designed to minimize the risk of subsynchronous oscillations, thereby ensuring a damped response at frequencies below the fundamental frequency of the power system.

Accordingly, the behavior of GFM converters—when viewed from the PCC—can be characterized in the frequency domain, as illustrated in Fig. 1. At low frequencies (typically up to 5 Hz, depending on the system requirements), determined by the bandwidth of the outer-control loops, the GFM converter should exhibit a constant-power behavior, i.e., the "slowly varying" voltage source should change its amplitude and phase in order to closely follow the active- and reactive-power setpoints. This frequency range is where the converter typically displays an active behavior [23].

At frequencies above this range and up to the system's fundamental frequency, the converter should exhibit a damped response to avoid harmful control interactions and mitigate the risk of subsynchronous resonances.

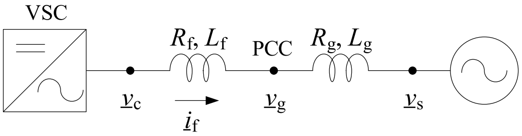

FIGURE 2. Single-line circuit diagram of the investigated network.

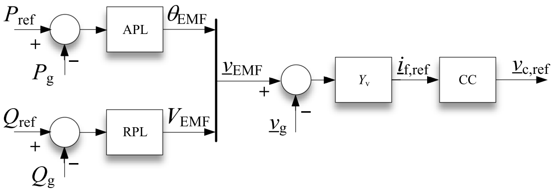

FIGURE 3. Generalized structure of VA-GFM control strategy.

In the harmonic range (i.e., at frequencies above the fundamental), the converter is expected to behave as a resistive–inductive impedance. The corresponding equivalent impedance seen from PCC is given by the sum of the physical filter impedance and any virtual impedance implemented in the controller. This enables the converter to act as a sink for harmonics, thereby improving power quality [3].

B. NEED FOR POWER DECOUPLING IN GFM CONVERTERS

Fig. 2 illustrates the single-line diagram of the network under investigation. The network consists of a voltage-source converter (VSC) system connected to an electrical AC grid through an RL filter, characterized by a resistance R_{f} and an inductance L_{f}. The AC grid is represented using its Thévenin equivalent, with R_{g} and L_{g} denoting the grid resistance and inductance, respectively. The VSC system assumes a constant DC-link voltage. The converter current vector is represented by $\underline{i}_{\mathrm{f}}$, while the voltage vectors at the PCC, the converter terminal, and the Thévenin equivalent voltage source are denoted by $\underline{v}_{\mathrm{g}}$, $\underline{v}_{\mathrm{c}}$, and $\underline{v}_{\mathrm{s}}$ respectively.

Fig. 3 illustrates the generic block diagram of the VA-GFM controller. In this configuration, the outer control loops—specifically the APL and the (RPL—compute the reference values for the virtual-voltage source, denoted as $\underline{v}_{\mathrm{EMF}}$. The APL regulates the active-power flow at the PCC, P_{g}, by adjusting the angle of the virtual voltage, θ_{EMF}. The RPL[1] determines the magnitude of the virtual-voltage source, V_{EMF}, to control the reactive-power flow at the PCC, Q_{g}. In this control scheme, the APL is responsible for tracking the reference-active power, P_{ref}, and for grid synchronization. Various configurations of the APL are possible, ranging from simple proportional controllers [8], [24] or proportional–integral (PI) controllers [25], to controllers that emulate the electromechanical dynamics of SM [6].

A key feature of VA-GFM control is that the outer loops directly calculate the voltage references—specifically, the

---

[1] Depending on the specific application, an AC-voltage controller may also be used.

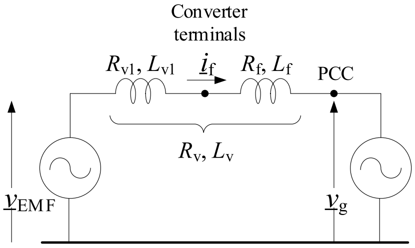

FIGURE 4. Equivalent circuit representation of VA-GFM.

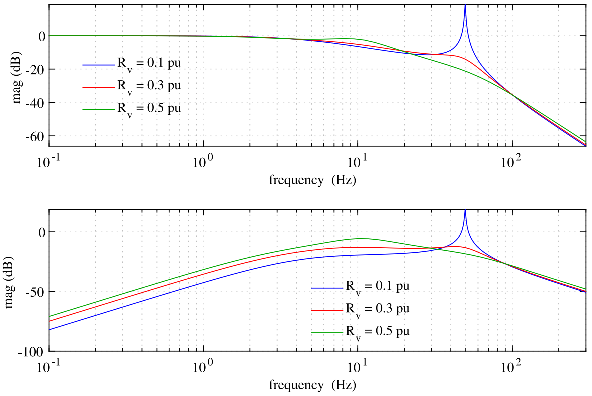

FIGURE 5. Top: magnitude of frequency response of $G_{\mathrm{APL}}(s)$ for VA-GFM; bottom: magnitude of frequency response of $G_{\mathrm{cp}}(s)$ for VA-GFM. Blue curves: $R_{\mathrm{v}} = 0.1$ p.u.; red curves: $R_{\mathrm{v}} = 0.3$ p.u.; green curves: $R_{\mathrm{v}} = 0.5$ p.u.

magnitude and phase angle of the emulated internal-voltage source. This distinguishes VA-GFM control from the more traditional GFL control, in which the outer loops calculate the current references for the inner-current controller (CC). Therefore, when GFL control is adopted, the converter can be represented as a controllable-current source, whose currents are determined by, for example, the power loops. Thus, in case of transients in the grid, the GFL will react to keep the converter's current constant. On the contrary, although VA-GFM control also employs a CC (see Fig. 3), the APL and RPL calculate the virtual-voltage $\underline{v}_{\mathrm{EMF}}$; in case of grid transients, the controller will react to keep this voltage constant, meaning that the converter can now be represented as a controllable-voltage source. The role of the CC is simply to track the current reference $\underline{i}_{\mathrm{f,ref}}$ calculated via the virtual impedance $\underline{Y}_{\mathrm{v}}$.

Fig. 4 illustrates the equivalent circuit of the converter employing VA-GFM control. The parameters R_{v} and L_{v} represent the equivalent resistance and inductance between the emulated voltage source and the PCC, respectively. These are referred to as virtual resistance and virtual inductance. As shown in the figure, the equivalent impedance consists of two components: a fixed part, determined by the physical converter-filter resistance and inductance, and a tunable virtual component, represented by R_{v1} and L_{v1}.

Fig. 5 (top figure) shows the magnitude of the frequency response of the closed-loop transfer function $G_{\mathrm{APL}}(s) = \frac{\Delta P_{\mathrm{g}}}{\Delta P_{\mathrm{ref}}}$ for the VA-GFM for different selections of the virtual resistance R_{v}. It can be observed that at very low frequencies, the gain is equal to 0 dB (1 p.u.), indicating proper setpoint tracking. At the same time, the transfer function exhibits a peak gain at frequencies around the fundamental (corresponding to 0 Hz in three phase). This resonance, addressed in the literature as synchronous-frequency resonance (SFR) [26], is typical for GFM controllers and originates from the natural response of the current flowing in an *RL* circuit when the resistive part is small. SFR in the converter's power output introduces a DC component in the converter current during operating-point changes. This poses a risk to the operation of equipment, such as transformers, and must be effectively damped. As shown in Fig. 5 (top figure), SFR can be attenuated by increasing the value of the virtual resistance R_{v}. On the other hand, an increase of R_{v} leads to a deterioration of the APL's closed-loop response and to a stronger coupling between the APL and RPL. This coupling can be analyzed by examining the transfer function from active-power reference variation to reactive-power variation, denoted as $G_{\mathrm{cp}}(s) = \frac{\Delta Q_{\mathrm{g}}}{\Delta P_{\mathrm{ref}}}$ for the VA-GFM control and depicted in Fig. 5 (bottom figure).

From the figure, it can be observed that increasing the virtual resistance raises the magnitude response of $G_{\mathrm{cp}}(s)$ across the low frequency range, indicating an increased coupling between the active- and reactive-power control loops. This behavior arises because an impedance with both inductive and resistive components causes both voltage angle and magnitude—the controlled quantities in GFM systems—to influence both active and reactive power, thereby introducing coupling. This can be understood more clearly by examining the quasi-steady-state power flow equations between two voltage sources.

Assuming a stiff grid connection, the power flow at the PCC in the investigated network (see Figs. 2 and 4) is given by

$$\underline{S}_{\mathrm{g}} = \underline{V}_{\mathrm{g}} \underline{I}_{\mathrm{f}}^{*} = \frac{\underline{V}_{\mathrm{g}} \underline{V}_{\mathrm{EMF}}^{*} - V_{\mathrm{g}}^{2}}{R_{\mathrm{v}} - J X_{\mathrm{v}}} \tag{1}$$

which yields to

$$P_{\mathrm{g}} = \frac{R_{\mathrm{v}} \left(V_{\mathrm{g}} V_{\mathrm{EMF}} \cos\delta - V_{\mathrm{g}}^{2} \right) + X_{\mathrm{v}} V_{\mathrm{g}} V_{\mathrm{EMF}} \sin\delta}{R_{\mathrm{v}}^{2} + X_{\mathrm{v}}^{2}} \tag{2}$$

$$Q_{\mathrm{g}} = \frac{-R_{\mathrm{v}} V_{\mathrm{g}} V_{\mathrm{EMF}} \sin\delta + X_{\mathrm{v}} \left(V_{\mathrm{g}} V_{\mathrm{EMF}} \cos\delta - V_{\mathrm{g}}^{2} \right)}{R_{\mathrm{v}}^{2} + X_{\mathrm{v}}^{2}} \tag{3}$$

where $\underline{V}_{\mathrm{g}} = V_{\mathrm{g}}\, \mathrm{e}^{J0}$ and $\underline{V}_{\mathrm{EMF}} = V_{\mathrm{EMF}}\, \mathrm{e}^{J\delta}$ are the phasors describing the two voltage sources, and $R_{\mathrm{v}} = R_{\mathrm{v1}} + R_{\mathrm{f}}$ and $X_{\mathrm{v}} = X_{\mathrm{v1}} + X_{\mathrm{f}}$ represent the (partially virtual) resistance and reactance, respectively, between these two sources. The superscript "$*$" in the notations refers to complex conjugate. Assuming a negligible resistance, the equations for active- and reactive-power flows become

$$P_{\mathrm{g}} = \frac{V_{\mathrm{g}} V_{\mathrm{EMF}} \sin\delta}{X_{\mathrm{v}}} \tag{4}$$

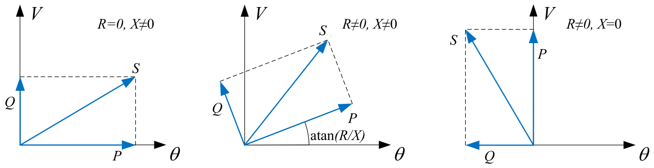

FIGURE 6. Impact of impedance angle on relation between voltage's amplitude and angle and active and reactive power [16].

and

$$Q_{\rm g} = \frac{V_{\rm g} V_{\rm EMF} \cos\delta - V_{\rm g}^2}{X_{\rm v}}. \tag{5}$$

For a constant PCC voltage, the linearized forms of (4) and (5) are

$$\Delta P_{\rm g} = \frac{V_{\rm g,0} V_{\rm EMF,0} \cos\delta_0 \Delta\delta + V_{\rm g,0} \sin\delta_0 \Delta V_{\rm EMF}}{X_{\rm v}} \tag{6}$$

$$\Delta Q_{\rm g} = \frac{-V_{\rm g,0} V_{\rm EMF,0} \sin\delta_0 \Delta\delta + V_{\rm g,0} \cos\delta_0 \Delta V_{\rm EMF}}{X_{\rm v}} \tag{7}$$

where the subscript "0" denotes the steady-state values. For a small δ_0, (6) and (7) simplify to

$$\Delta P_{\rm g} \approx \frac{V_{\rm g,0} V_{\rm EMF,0}}{X_{\rm v}} \Delta\delta \tag{8}$$

$$\Delta Q_{\rm g} \approx \frac{V_{\rm g,0}}{X_{\rm v}} \Delta V_{\rm EMF}. \tag{9}$$

Equations (8) and (9) clearly reveal the dependence of active power on voltage angle and reactive power on voltage magnitude, which forms the fundamental basis of GFM control. However, as the R/X-ratio increases, this simplification becomes increasingly inaccurate. For a predominantly resistive impedance, the previously stated relation is reversed, resulting in the active power being determined mainly by voltage magnitude, and reactive power by voltage angle. The linearized expressions for this case are

$$\Delta P_{\rm g} \approx \frac{V_{\rm g,0}}{R_{\rm v}} \Delta V_{\rm EMF} \tag{10}$$

$$\Delta Q_{\rm g} \approx \frac{-V_{\rm g,0} V_{\rm EMF,0}}{R_{\rm v}} \Delta\delta. \tag{11}$$

These relations are illustrated in Fig. 6 [16]. Consequently, an impedance with nonnegligible inductive and resistive components causes both controlled quantities—voltage angle and magnitude—to influence both power components, leading to power coupling. This phenomenon is undesirable, as it degrades controller performance during both small and large transients in the grid. Most controller designs are based on the assumption of a purely reactive system, where power decoupling holds true—an assumption that is appropriate for high-voltage transmission systems, where line losses are negligible. In this case, the simplified power flow equations given by (4) and (5) are valid. However, when virtual resistance is increased, power coupling is introduced, limiting the feasible values of $R_{\rm v}$ to relatively small magnitudes in VA-GFM control. To address this challenge, the control strategy proposed in this aricle allows the virtual resistance to be freely selected to effectively damp SFR without introducing coupling between the power control loops, as demonstrated in Section IV.

III. DECOUPLED VA-GFM CONTROL

Fig. 7 shows the block diagram of the proposed Decoupled VA-GFM control. The controller, implemented in the stationary $\alpha\beta$-plane, is based on the VA-GFM in Fig. 3, where the power controllers directly generate the back-electromotive force (EMF) voltage, $\underline{v}_{\rm EMF}$. As a main difference, in the proposed approach the complex signal $\underline{\kappa}$ formed by the outputs of the APL and RPL, is passed through a phase-compensation block that compensates for the power coupling introduced by the virtual admittance $\underline{Y}_{\rm v}$.The phase compensation allows the selection of arbitrary values for virtual resistance and inductance while maintaining near-perfect decoupling between the APL and RPL in the frequency region where these controllers are active. Note that although the APL and RPL work independently, differently from any other VA-GFM implementation they share the same control structure; thus, if the same loop bandwidth for the APL and RPL is selected, the controller is symmetric and can be represented through a single-input/single-output transfer function.

A. VA PHASE COMPENSATION

A key element of the proposed controller is the VA phase compensation applied to the output of the APL and RPL. The decoupling is achieved by dynamically rotating the complex signal $\underline{\kappa}$ by the frequency-dependent virtual-admittance angle, $\varphi_{\rm Y}(s)$ as shown in Fig. 8. Consequently, the resulting power flow appears as if governed by a purely resistive network, where voltage magnitude controls active power and voltage-phase angle controls reactive power (see Fig. 6). Conceptually, the VA phase compensation proposed here is similar to the method proposed in [16], as it rotates the complex-apparent power vector to remove the coupling introduced by generic RL impedance. However, it is important to note that the dynamic implementation proposed here applies not only to the fundamental frequency, but to the entire frequency range where the power controllers are active, i.e., the "constant-power" frequency range in Fig. 1. This is achieved through the dynamic implementation of the virtual-admittance, $Y_{\rm v}(s)$, in the phase-compensation block.

The decoupling mechanism can be illustrated in steps using the circuit in Fig. 4 and the phase-compensation block in Fig. 8. For a generic system frequency ω and using a rotating-frame synchronized with the grid-voltage, the two voltage phasors can be represented as $\underline{V}_{\rm EMF}(\omega) = V_{\rm EMF}\, e^{J\delta}$and $\underline{V}_{\rm g}(\omega) = V_{\rm g}\, e^{J0^\circ}$, which are connected by the admittance $\underline{Y}_{\rm v}(\omega) = \frac{1}{R_{\rm v}+J\omega L_{\rm v}} = Y_{\rm v}\, e^{J\varphi_{\rm Y}}$. This allows to express

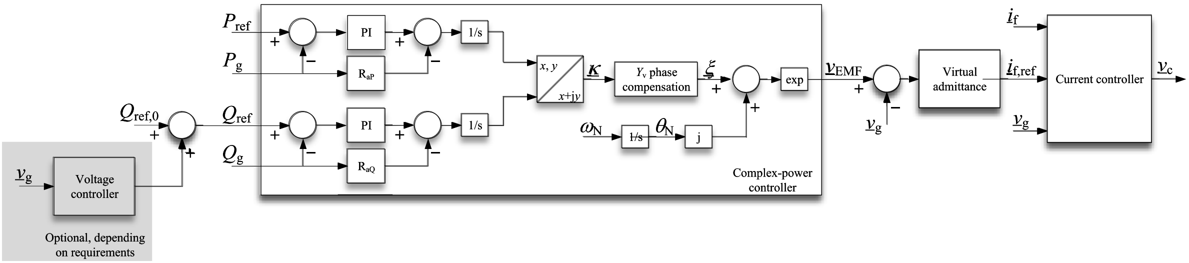

FIGURE 7. Block diagram of the proposed decoupled GFM control, including detailed description of the apparent-power controller.

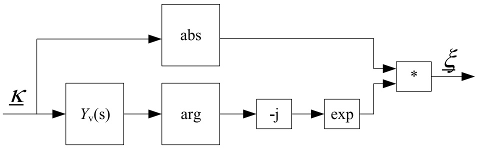

FIGURE 8. Implemented VA phase compensation.

the complex-apparent power at $\underline{V}_g$ as

$$\begin{aligned}\underline{S}_g(\omega) &= \underline{V}_g(\omega)\underline{I}_f^*(\omega)\\ &= V_g Y_v\, e^{-J\varphi_Y}(V_{EMF}\, e^{-j\delta} - V_g).\end{aligned} \tag{12}$$

As clearly indicated in (12), the power flow is dependent on the phase of the virtual admittance and hence a coupling exists for the conventional approach. The proposed scheme generates the voltage $\underline{v}_{EMF}$ so that the power flow is not dependent on φ_Y. This is equivalent of rotating the power phasor by φ_Y to obtain

$$\underline{S}_{g,shift}(\omega) = V_g Y_v (V_{EMF}\, e^{-j\delta} - V_g) \tag{13}$$

which is the power flow over a frequency-dependent resistive admittance $Y_v = (R_v^2 + (\omega L_v)^2)^{-1/2}$. Consequently, the rotation of the complex-power phasor cancels the coupling effect of the complex admittance $\underline{Y}_v(\omega)$.

Following the details of Figs. 7 and 8, the phasor $\underline{V}_{EMF}$ is given by

$$\underline{V}_{EMF} = e^{\underline{\xi}} = e^{|\underline{\kappa}|e^{-j(\varphi_Y + \angle\underline{\kappa})}} = e^{\underline{\kappa}^* e^{-j\varphi_Y}} \tag{14}$$

or, in terms of voltage perturbation

$$\Delta\underline{V}_{EMF} = \left(\underline{V}_{EMF,0}\, e^{-j\varphi_Y}\right)\Delta\underline{\kappa}^*. \tag{15}$$

Assuming a stiff grid voltage, the power flow variation resulting from the voltage perturbation is

$$\begin{aligned}\Delta\underline{S}_g(\omega) &= V_{g,0} Y_v e^{-j\varphi_Y}\left[\left(\underline{V}_{EMF,0}\, e^{-j\varphi_Y}\right)\Delta\underline{\kappa}^*\right]^*\\ &= V_{g,0} Y_v \underline{V}_{EMF,0}^* \Delta\underline{\kappa}.\end{aligned} \tag{16}$$

It can be understood from (16) that the power output is dictated strictly by the outputs of the power controllers where the impact of the virtual-admittance phase is canceled by the phase compensation unit, similar to the rotated power expression in (13) and unlike the conventional approach as in (12).

As illustrated in Fig. 6 and visible by linearizing (13), reactive power is determined by the negative voltage phase angle for the resulting purely resistive case. To maintain the same sign for both components, the proposed VA phase compensation multiplies the angle of the (unshifted) complex-power vector with −1, which corresponds to mirroring the vector on the V-axis of the resistive case in Fig. 6.

It is of importance to stress that the phase rotation (and thereby the decoupling) is applied to the complex signal $\underline{\kappa}$ and impacts the design of the APL and RPL only. After calculation of the virtual voltage $\underline{v}_{EMF}$, active- and reactive- power flows are governed by the system voltage and the actual virtual impedance. The choice of a phase rotation that results in a resistive representation of the virtual impedance is made due to the fact that this allows for a complex representation of the inputs to the power controller (from this the use of the terminology *complex-power controller*). As it can be easily understood, a similar approach can be adopted where the phase compensation leads to a purely reactive representation of the virtual impedance, leading to a more classical approach. The duality in the selection of a resistive or reactive representation for the virtual impedance is given in Appendix.

Note that the VA phase compensation can be applied at the input of the power controllers, as is, for example, the case in [16]. If the control parameters of both power control loops are chosen to be identical, this configuration results in behavior equivalent to applying the compensation at the controller outputs, as illustrated in Fig. 7. However, applying the compensation at the controller outputs allows the APL and RPL to be tuned independently, as demonstrated in the following section. In contrast, placing the compensation at the controller inputs causes both APL and RPL to jointly regulate active and reactive power in proportion to the ratio between R_v and L_v, that is, according to the VA angle φ_Y. Therefore, when independent tuning of the APL and RPL is desired—for instance, to provide inertial support by slowing down only the APL—the phase compensation should be applied at the controller outputs, as proposed here.

B. DERIVATION OF DECOUPLED VA-GFM CONTROL PARAMETERS

1) TUNING OF COMPLEX-POWER CONTROLLER

The complex-power controller provides both complex power-reference tracking as well as grid-voltage synchronization.

The complex-power controller proposed here has identical structure for active and reactive power, consisting of a PI controller and an active damping term (see Fig. 7). The tuning of the controller is detailed below and is similar to the loop shaping approach described in [27].

Assuming initial conditions for the grid voltage $V_{g,0} = 1$ per unit (p.u.) and, for simplicity of the derivation, $P_{ref} = Q_{ref} = 0$ p.u., the initial condition for the internal voltage $\underline{V}_{EMF}$ becomes $\underline{V}_{EMF,0} = V_{g,0} = 1$ p.u.. Using these assumptions, (16) and $\Delta\underline{\kappa} = \Delta\gamma + J\Delta\varepsilon$, the linearized active and reactive powers can be expressed as

$$\Delta P_g = Y_v \Delta\gamma \tag{17}$$

$$\Delta Q_g = Y_v \Delta\varepsilon. \tag{18}$$

Following Fig. 7 the control laws for the APL and RPL are given as

$$\gamma = \frac{1}{s}\left[\left(K_{pP} + \frac{K_{iP}}{s}\right)(P_{ref} - P_g) - R_{aP}P_g\right] \tag{19}$$

$$\varepsilon = \frac{1}{s}\left[\left(K_{pQ} + \frac{K_{iQ}}{s}\right)(Q_{ref} - Q_g) - R_{aQ}Q_g\right] \tag{20}$$

and the closed-loop transfer function from the active-power reference to the active power can be expressed as

$$G_{P_{ref}\to P_g} = \frac{\Delta P_g}{\Delta P_{ref}} = \frac{Y_v(K_{pP}s + K_{iP})}{s^2 + (R_{aP} + K_{pP})s + K_{iP}}. \tag{21}$$

An equivalent expression can be derived for $G_{Q_{ref}\to Q_g}$. This transfer function can be loop-shaped to second-order low-pass filter (LPF) by selecting the following control parameters:

$$\begin{aligned} K_{p,P} &= \alpha_P [Y_v(\omega_N)]^{-1} \\ K_{i,P} &= \alpha_P^2 [Y_v(\omega_N)]^{-1} \\ R_{a,P} &= \alpha_P(2\zeta_P - 1)[Y_v(\omega_N)]^{-1} \end{aligned} \tag{22}$$

where α_P is the desired loop bandwidth, ζ_P the desired damping ratio and the magnitude of the virtual admittance at rated frequency, and $Y_v(\omega_N) = (R_v^2 + \omega_N^2 L_v^2)^{-1/2}$ is used for calculating the control gains. Selecting $\zeta_P = 1$, yields to a closed-loop system shaped as a first-order LPF.

The parameters for the RPL are tuned equivalently, and are determined by the selection of the desired loop bandwidth α_Q and damping ratio ζ_Q. In the case that the loop bandwidths and damping ratios for the APL and RPL are selected to be the same, both transfer functions can be expressed through a single, real-valued transfer function for the complex-apparent power

$$G_{S_{ref}\to S_g} = \frac{\Delta\underline{S}_g}{\Delta\underline{S}_{ref}} = \frac{\alpha\,(s+\alpha)}{s^2 + 2\zeta\alpha + \alpha^2}. \tag{23}$$

2) α_P-SELECTION FOR INERTIA PROVISION

As shown in [28], the APL in the proposed design can be tuned to provide an inertial response equivalent to that of a SM or a virtual SM, i.e. a GFM converter implementing the SM's mechanical equation as its active-power control law. The closed-loop transfer function from grid-voltage angle θ_g to active power is given as

$$G_{\theta_g\to P} = \frac{X_v Y_v^2 s^2}{s^2 + \alpha_P\zeta_P s + \alpha_P^2}. \tag{24}$$

Based on this, the inertial response can be estimated as $s \to 0$ by

$$G_{\dot{\omega}_g\to P} = \frac{G_{\theta_g\to P}}{s^2} = \frac{X_v Y_v^2}{s^2 + \alpha_P\zeta_P s + \alpha_P^2} = P_H. \tag{25}$$

The inertial response relates to the provided inertia-time constant as $H = P_H\frac{\omega_N}{2}$ [28], yielding to

$$\alpha_P = \sqrt{\frac{X_v[Y_v(\omega_N)]^2}{H}\,\frac{\omega_N}{2}}. \tag{26}$$

TABLE 1. System and Control Parameters for the Frequency Analysis

System parameters		Control parameters	
S_N	100 MVA	L_{v1}	0.35 p.u.
V_N	33 kV	R_{v1}	0.485 p.u.
ω_b	314.16 rad/s	$\alpha_P = \alpha_Q$	2π 5 rad/s
L_f	0.15 p.u.	$\zeta_P = \zeta_Q$	1
R_f	0.015 p.u.	α_{CC}	2π 200 rad/s
SCR	3 p.u.		

IV. FREQUENCY ANALYSIS

As argued in Section II, the frequency domain analysis of the converter's behavior is an indispensable tool to ensure compliance with grid code requirements and demonstrate some of the GFM properties, e.g., absence of adverse control interactions. Taking into account that the time constant of the VA is selected to be much smaller than that of the outer APL and RPL, a first analysis is made using the steady-state representation of the VA (as it is often the case in works dealing with analysis of VA-GFM available in the literature). This is followed by an analysis including the dynamics introduced by the virtual inductance, to highlight differences and the impacts of control parameters. The system and control parameters used for this analysis are shown in Table 1, with deviating values mentioned in the text.

A. ANALYSIS WITH STEADY-STATE VA REPRESENTATION

Consider the steady-state representation of the VA, $\underline{Y}_{v,ss} = (R_v + JX_v)^{-1}$, and assume a fast and accurate CC. The Bode diagram of the transfer function from reference- to actual-complex power for the tuning provided in the previous section is displayed in Fig. 9 and shows the expected LPF-behavior as well as the absence of any coupling between active and reactive power.

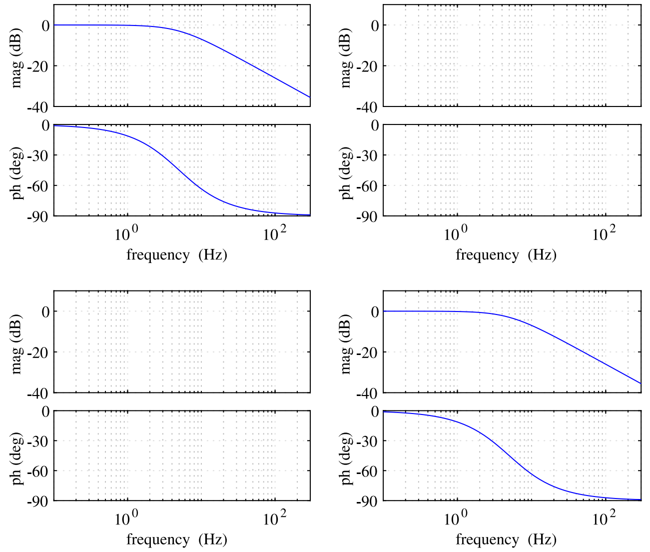

FIGURE 9. **Closed-loop response of decoupled GFM controller. Virtual reactor dynamics neglected. Top left: P_{ref} to P_g; Top right: Q_{ref} to P_g; Bottom left: P_{ref} to Q_g; Bottom right: Q_{ref} to Q_g.**

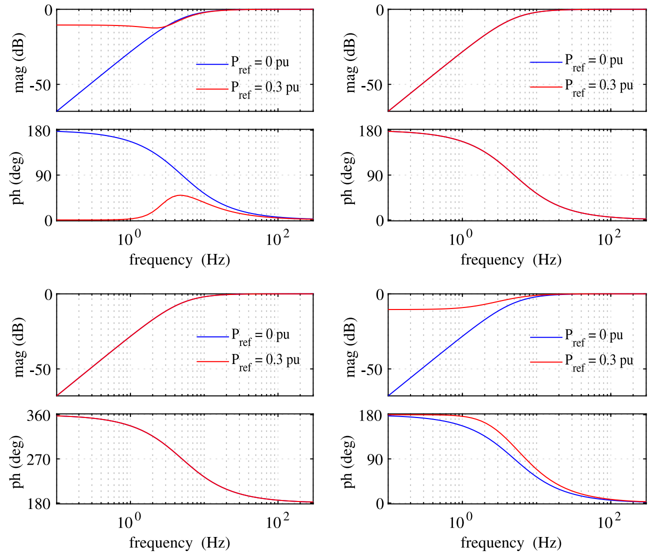

FIGURE 10. **Input admittance of decoupled GFM controller. Virtual reactor dynamics neglected. Blue curves: $P_{ref} = Q_{ref} = 0$ pu; red curves: $P_{ref} = 0.3$ p.u., $Q_{ref} = 0$ p.u. Top left: $Y_{c,ss}^{dd}$; Top right: $Y_{c,ss}^{dq}$; Bottom left: $Y_{c,ss}^{qd}$ Bottom right: $Y_{c,ss}^{qq}$.**

Under the same assumptions, the converter's input admittance is given as

$$\begin{bmatrix}\Delta i_{\mathrm{f}}^{\mathrm{d}}\\ \Delta i_{\mathrm{f}}^{\mathrm{q}}\end{bmatrix} = -\underbrace{\begin{bmatrix} Y_{\mathrm{c,ss}}^{\mathrm{dd}}(s) & Y_{\mathrm{c,ss}}^{\mathrm{dq}}(s)\\ Y_{\mathrm{c,ss}}^{\mathrm{qd}}(s) & Y_{\mathrm{c,ss}}^{\mathrm{qq}}(s)\end{bmatrix}}_{\mathbf{Y}_{\mathrm{c,ss}}(s)} \begin{bmatrix}\Delta v_{\mathrm{g}}^{\mathrm{d}}\\ \Delta v_{\mathrm{g}}^{\mathrm{q}}\end{bmatrix} \tag{27}$$

with

$$\begin{aligned}
Y_{\mathrm{c,ss}}^{\mathrm{dd}}(s) &= \frac{P_{\mathrm{ref}}}{V_{\mathrm{g},0}^2}\frac{\alpha_{\mathrm{P}}(\alpha_{\mathrm{P}}+2s)}{(s+\alpha_{\mathrm{P}})^2} + \frac{R_{\mathrm{v}}}{R_{\mathrm{v}}^2+X_{\mathrm{v}}^2}\frac{s^2}{(s+\alpha_{\mathrm{P}})^2}\\
Y_{\mathrm{c,ss}}^{\mathrm{dq}}(s) &= -\frac{Q_{\mathrm{ref}}}{V_{\mathrm{g},0}^2}\frac{\alpha_{\mathrm{P}}(\alpha_{\mathrm{P}}+2s)}{(s+\alpha_{\mathrm{P}})^2} + \frac{X_{\mathrm{v}}}{R_{\mathrm{v}}^2+X_{\mathrm{v}}^2}\frac{s^2}{(s+\alpha_{\mathrm{P}})^2}\\
Y_{\mathrm{c,ss}}^{\mathrm{qd}}(s) &= -\frac{Q_{\mathrm{ref}}}{V_{\mathrm{g},0}^2}\frac{\alpha_{\mathrm{Q}}(\alpha_{\mathrm{Q}}+2s)}{(s+\alpha_{\mathrm{Q}})^2} - \frac{X_{\mathrm{v}}}{R_{\mathrm{v}}^2+X_{\mathrm{v}}^2}\frac{s^2}{(s+\alpha_{\mathrm{Q}})^2}\\
Y_{\mathrm{c,ss}}^{\mathrm{qq}}(s) &= -\frac{P_{\mathrm{ref}}}{V_{\mathrm{g},0}^2}\frac{\alpha_{\mathrm{Q}}(\alpha_{\mathrm{Q}}+2s)}{(s+\alpha_{\mathrm{Q}})^2} + \frac{R_{\mathrm{v}}}{R_{\mathrm{v}}^2+X_{\mathrm{v}}^2}\frac{s^2}{(s+\alpha_{\mathrm{Q}})^2}.
\end{aligned} \tag{28}$$

The components of the converter's admittance $\mathbf{Y}_{\mathrm{c,ss}}$ reveal that the Decoupled GFM very well follows the desired frequency behavior depicted in Fig. 1. Each impedance component is constituted by two terms: the first term depends on the desired active/reactive setpoint and has a LPF shape, identifying the "constant power" region in Fig. 1. Note that (28) also gives the possibility to easily assess the passivity properties of the converter. This is particularly helpful in the constant-power region, i.e. for $\omega \ll \alpha_{\mathrm{P}}, \alpha_{\mathrm{Q}}$, where the converter typically exhibits a nonpassive behavior. For $s = 0$, the passivity-index of $\mathbf{Y}_{\mathrm{c,ss}}$ is equal to $-\sqrt{P_{\mathrm{ref}}^2 + Q_{\mathrm{ref}}^2}/V_{\mathrm{g},0}^2$ [29], which can be directly calculated from (28).

The second term presents a high-pass filter characteristic and only depends on the selected values for the virtual impedance. From (28), it can also be observed that the diagonal elements of $\mathbf{Y}_{\mathrm{c,ss}}$ only depend on the active-power setpoint, while the anti-diagonal elements depend on the reactive one. This confirms the effectiveness of the power decoupling action in case of power setpoints variation. At higher frequencies (where the impact of the APL and RPL vanishes), active- and reactive-power flow will only depend on the virtual admittance parameters, with a natural coupling determined by the virtual-impedance angle.

The expression in (27) can be further simplified for the case that the same bandwidth is selected for both power-control loops, $\alpha_{\mathrm{P}} = \alpha_{\mathrm{Q}} = \alpha$. In this case, $\mathbf{Y}_{\mathrm{c,ss}}$ becomes Hermitian and can be written as a complex expression[2] instead

$$\Delta \underline{i}_{\mathrm{f}}^{(\mathrm{dq})} = -\frac{R_{\mathrm{v}} - JX_{\mathrm{v}}}{R_{\mathrm{v}}^2+X_{\mathrm{v}}^2}\frac{s^2}{(s+\alpha)^2}\Delta \underline{v}_{\mathrm{g}}^{(\mathrm{dq})}. \tag{29}$$

Fig. 10 contains the Bode diagram for the converter's input admittance in (27), for different setpoints. The constant power and constant admittance[3] behaviors are clearly visible. The transition between these depends on the selected loop-bandwidths for the APL and RPL.

B. ANALYSIS WITH DYNAMIC VA REPRESENTATION

For a complete analysis, it is necessary to take the dynamics of the VA into account. In Fig. 11, the Bode diagram of the

---

[2] Similar to the constant-power region, the converter's passivity properties in the constant-impedance region can be assessed using (29) for $\omega \gg \alpha$.

[3] As the steady-state representation is chosen here, the admittance's frequency dependency is not represented in these figures.

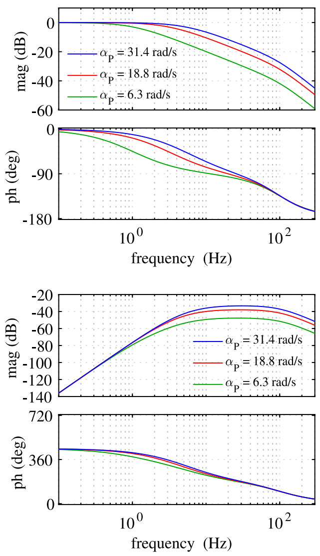

FIGURE 11. Closed-loop response of decoupled GFM controller for different values of α_P. Virtual reactor dynamics included. Top left: P_{ref} to P_g; Top right: Q_{ref} to P_g; Bottom left: P_{ref} to Q_g; Bottom right: Q_{ref} to Q_g. Green curves: $\alpha_P = 1 \cdot 2 \cdot \pi$ rad/s; Red curves: $\alpha_P = 3 \cdot 2 \cdot \pi$; Blue curves: $\alpha_P = 5 \cdot 2 \cdot \pi$.

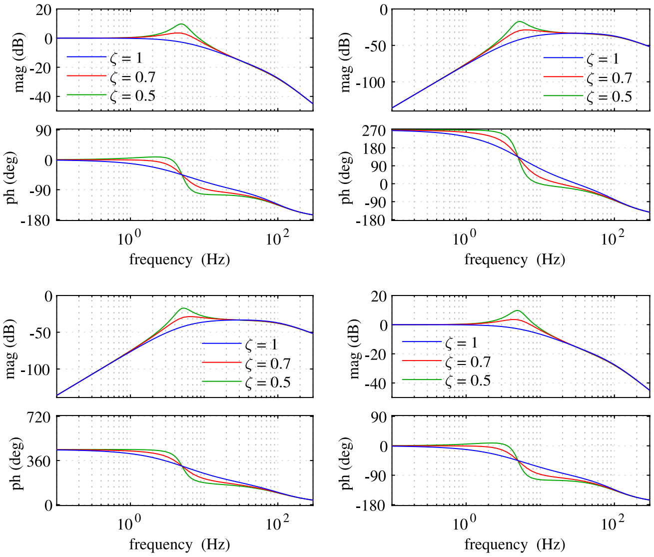

FIGURE 12. Closed-loop response of decoupled GFM controller for different values of damping ζ in the power-control loops; $\zeta_P = \zeta_Q = \zeta$. Virtual reactor dynamics included. Green curves: $\zeta = 0.5$; Red curves: $\zeta = 0.7$; Blue curves: $\zeta = 1$. Top left: P_{ref} to P_g; Top right: Q_{ref} to P_g; Bottom left: P_{ref} to Q_g; Bottom right: Q_{ref} to Q_g.

closed-loop transfer function including the frequency dynamics is shown for different values of the APL bandwidth α_P for $P_{\text{ref}} = Q_{\text{ref}} = 0$. The impact of the VA frequency dynamics can be seen when comparing the blue curves to Fig. 9. Even with those dynamics, the LPF-behavior of the response is preserved. As a main difference, it can be observed that the coupling between Q_{ref} and P_g as well as between P_{ref} and Q_g, respectively, is nonzero but remains very small, especially in the frequency region where the APL and RPL are active. The effectiveness of the proposed decoupled GFM can be further appreciated when comparing with the frequency response for the conventional VA-GFM for the same selection of the virtual resistance R_V (see Fig. 5, green curves). Besides the small coupling, it is important to observe that the Decoupled GFM allows to preserve the desired closed-loop response, despite of the large selection of R_V. Comparing the curves representing different loop bandwidths in Fig. 11 shows that reducing α_P leads to a faster decay of the gain as expected, resulting in a narrower frequency range with constant-power behavior. It can also be seen that the change of α_P does not have an impact on the reactive-power response Q_{ref} to Q. Manipulating the RPL's α_Q gives equivalent results,[4] and in particular no impact on the active-power response.

In Fig. 12, the impact of the damping ratio on the frequency response of the APL and RPL can be studied. A reduction of the damping ratio ζ from 1 (blue) over 0.7 (red) to 0.5 (green) results in an amplification at frequencies around α_P and α_Q.

The same effects can be seen in Fig. 13, showing the converter's input admittance for changing damping ratios ζ under consideration of the VA frequency dynamics. As a main difference compared to the case depicted in Fig. 10, the frequency dynamics become visible as a decaying magnitude in the high frequency range, caused by the growing impact of the term sL_V.[5] The amplification caused by low damping

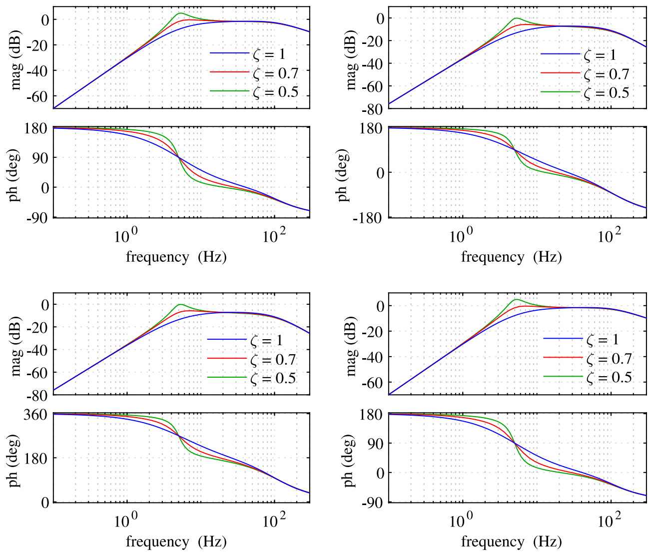

FIGURE 13. Input admittance of decoupled GFM controller for different values of damping ζ in the power-control loops; $\zeta_P = \zeta_Q = \zeta$. Virtual reactor dynamics included. Top left: Y_{dd}; Top right: Y_{dq}; Bottom left: Y_{qd} Bottom right: Y_{qq}. Green curves: $\zeta = 0.5$; Red curves: $\zeta = 0.7$; Blue curves: $\zeta = 1$.

---

[4] The corresponding figure is not shown here due to space constraints

[5] It can be proven that components of the converter's input admittance can be well approximated to the ones in (28) by considering the frequency-dependent model of the VA in the derivation of the second right-hand terms.

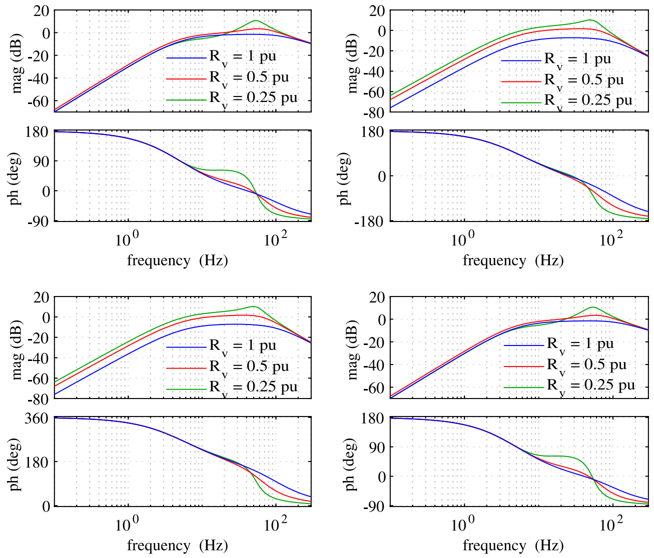

FIGURE 14. Input admittance of decoupled GFM controller for different values of the virtual resistance R_v. Virtual reactor dynamics included. Top right: Y_{dq}; Bottom left: Y_{qd} Bottom right: Y_{qq}. Green curves: $R_v = 0.25$ p.u.; Red curves: $R_v = 0.5$ p.u.; Blue curves: $R_v = 1$ p.u.

ratios in the power controllers is also replicated in the input admittance, which makes it clear that this parameter has a large impact on the provision of damping at frequencies close to the loop bandwidth of the power controllers. This is particularly relevant if the converter system is required to dampen power-system oscillations, which often appear in this frequency region.

As expected from the analysis in Section II, changing the virtual resistance, R_v, mainly has an impact on the damping in the subsynchronous-frequency range and particularly at the SFR, which lies at 50 Hz. This is visible in Fig. 14, which shows the input admittance for different values of R_v.

The inertial response provided by the APL can be examined with help of the frequency response from grid voltage frequency derivative $\mathrm{d}f/\mathrm{d}t$ to active power P_g, shown in Fig. 15. As can be seen from the figure, a higher inertia constant, corresponding to a lower α_P, results in a higher gain, which corresponds to a larger inertial response.

To summarize, the frequency analysis of the decoupled GFM controller shows that the proposed design addresses both the problem of SFR as well as power coupling, as demonstrated by the presented frequency responses. It has furthermore shown how different control parameters can be used to influence the controller response in different frequency ranges. These findings are summarized in Fig. 16, which shows the dd-element of the converter's input admittance as a comparison to the desired converter behavior shown in Fig. 1. For comparison, the response of a pure admittance, without controller, is also shown in black. From the figure, it can be seen that the main difference to the pure admittance appears for frequencies around and below the APL's and RPL's bandwidth, as the converter shows a constant power behavior in this range. As can be seen from the dashed green curve, the main way to impact the controller's response at frequencies around the power controller's loop bandwidth (apart from tuning the controller's parameters to a different bandwidth) is the damping ratio ζ. At higher frequencies (here up to about 100 Hz) and in particular around the fundamental, the virtual resistance R_v becomes the dominant factor. This parameter also plays the main role in the damping of the SFR. For frequencies above this, the main impact on the input admittance gradually shifts from R_v to the virtual inductance L_v, until the bandwidth limitation of the CC deteriorates the representation of the VA.

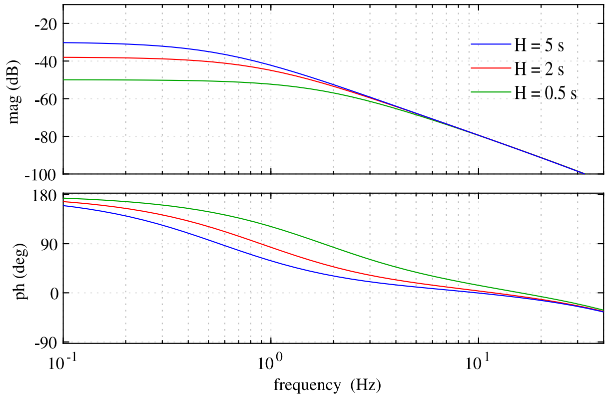

FIGURE 15. Frequency response of decoupled GFM controller from grid frequency derivative to P_g for different values of inertia-time constant H. Virtual reactor dynamics included. Green curves: $H = 0.5$ s; red curves: $H = 2$ s; blue curves: $H = 5$ s.

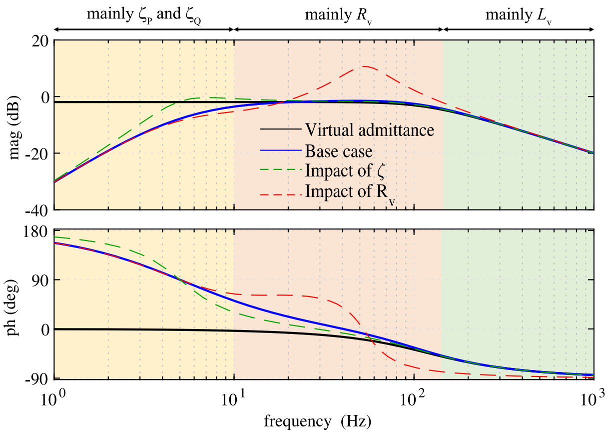

FIGURE 16. Comparison of Y_{dd} of virtual admittance and decoupled GFM controller. Virtual reactor dynamics included. $L_v = 0.5$ p.u. Solid black curves: virtual admittance response, with $R_v = 1$ p.u; solid blue curves: GFM controller response, with $R_v = 1$ p.u. and $\zeta_P = \zeta_Q = 1$ (base case). Dashed green curves: GFM controller response, with $R_v = 1$ p.u. and $\zeta = 0.7$; Dashed red curves: GFM controller response, with $R_v = 0.25$ p.u. and $\zeta = 1$.

V. EXPERIMENTAL VALIDATION

To validate the claimed performance of the controller, experimental validations have been carried out in the laboratory.

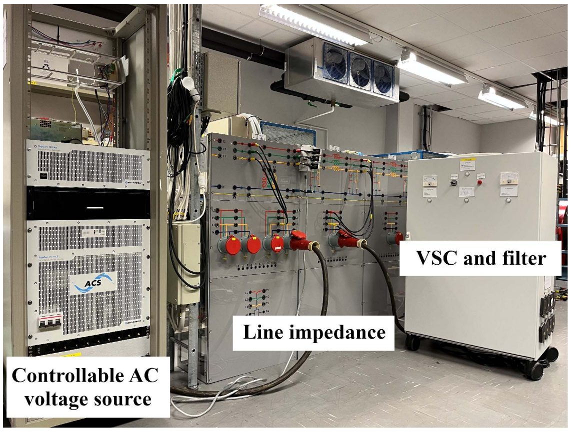

FIGURE 17. **Photo of the laboratory setup used for validation.**

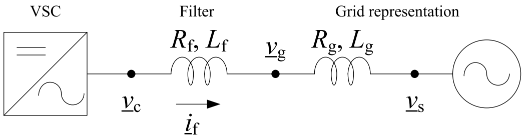

FIGURE 18. **Single-line diagram of the laboratory setup.**

TABLE 2. **System and Control Parameters for the Laboratory Setup**

System parameters		Control parameters	
S_N	1 kVA	L_v1	0.343 p.u.
V_N	100 V	R_v1	variable
ω_b	314.16 rad/s	$\alpha_\mathrm{P} = \alpha_\mathrm{Q}$	2π 5 rad/s
L_f	0.157 p.u.	$\zeta_\mathrm{P} = \zeta_\mathrm{Q}$	1
R_f	0.0157 p.u.	α_CC	2π 200 rad/s
SCR	variable	f_sampling	5 kHz

A photo of the laboratory setup is shown in Fig. 17, with the single-line diagram in Fig. 18. The grid voltage is emulated using a four-quadrant programmable AC power source by REGATRON, and the grid impedance is realized with the help of physical reactors. The GFM converter system consists of a two-level VSC supplied by an ideal DC voltage source rated at 300 V. The VSC is controlled using a dSPACE dS1006 real time controller, and is connected to the PCC through a phase reactor with inductance L_f and resistance R_f. Sinusoidal pulsewidth modulation is used to calculate the converter's switching pattern. The remaining system and control parameters used for the experimental validation are listed in Table 2. The APL and RPL bandwidths are chosen to comply with the recommendations for GFM control action defined in [21]. After grid energization, the VSC is initially operated via a simple GFL control scheme, consisting of a CC with zero-reference currents and a phase-locked loop for grid synchronization. Subsequently, the control strategy is switched to the proposed decoupled GFM controller.

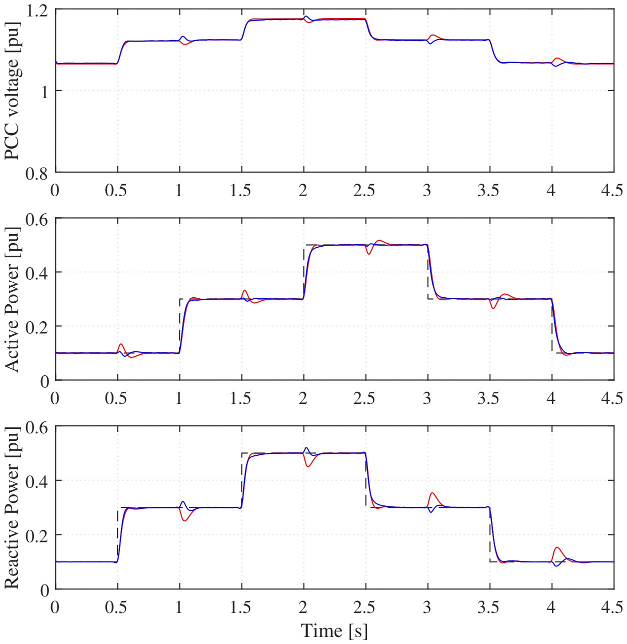

FIGURE 19. **Dynamic performance of proposed decoupled GFM controller (blue curves) and conventional VA-GFM (red curves) in case of steps in active- and reactive-power references (dashed-black curves). SCR = 3 and R_v = 0.5 p.u. Top: measured amplitude of PCC voltage; middle: measured active power; bottom: measured reactive power.**

Figs. 19 and 20 show the dynamic performance of the proposed decoupled GFM controller in reaction to steps in the active- and reactive-power references for a relatively weak grid with a short-circuit ratio (SCR) of 3, and for a stronger grid with a SCR of 5, respectively.Following the frequency analysis in Fig. 5, in order to suppress the SFR without the aid of additional controllers, the virtual resistance is set equal to the virtual reactance: $R_\mathrm{v} = L_\mathrm{v} = 0.5$ p.u. As shown, regardless of the strength of the connecting grid, the controller works as intended and presents a first-order LPF response as for the design. Only a small cross-coupling between active and reactive powers can be observed, mainly due to the variation of the grid voltage in response to a power step. For comparison, the dynamic performance of the conventional VA-GFM with the same control parameters and grid conditions is also reported in the figures (red curves).

In order to further appreciate the effectiveness of the proposed decoupled GFM controller against the conventional VA-GFM, Fig. 21 shows the detail of the dynamic performance of these controllers for two extreme selections of the virtual resistance: $R_\mathrm{v} = 0.3$ p.u. (dashed curves) and $R_\mathrm{v} = 1$ p.u. (solid curves). It is evident from the figure that the conventional VA-GFM presents a very large overshoot as the virtual resistance increases, up to c.ca 35% of the applied power step. On the other hand, the coupling between active and reactive powers is almost negligible when using the decoupled GFM, up to 4% for $R_\mathrm{v} = 1$ p.u. Furthermore, it is of importance to highlight that the dynamic performance of the decoupled GFM is almost unchanged regardless of the large variation in the virtual resistance, confirming the possibility of independent selection of the virtual impedance's parameters.

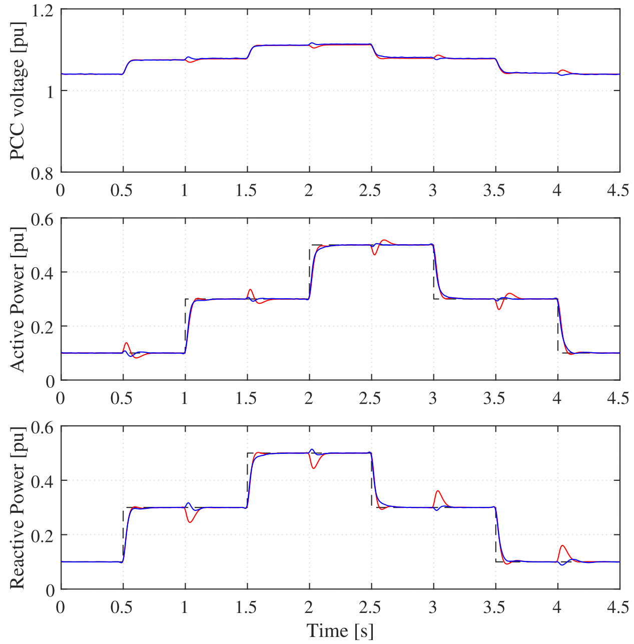

FIGURE 20. Dynamic performance of proposed decoupled GFM controller (blue curves) and conventional VA-GFM (red curves) in case of steps in active- and reactive-power references (dashed-black curves). SCR = 5 and $R_v = 0.5$ p.u. Top: measured amplitude of PCC voltage; middle: measured active power; bottom: measured reactive power.

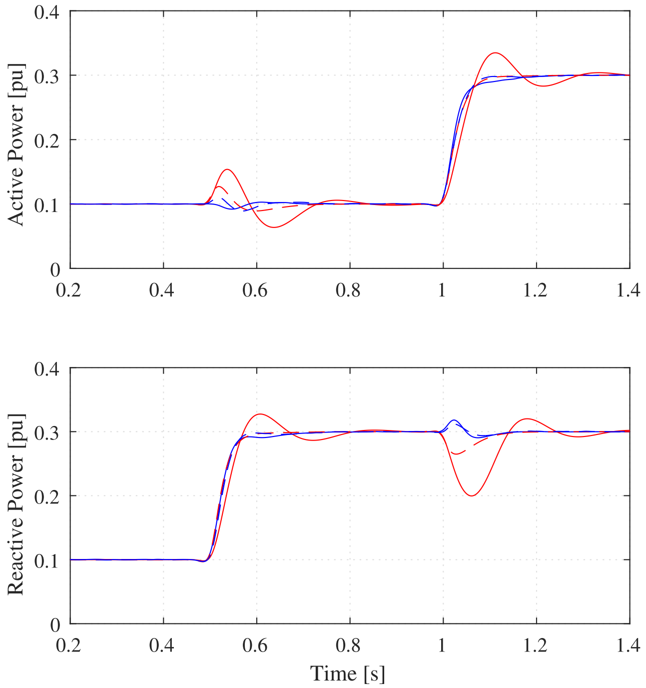

FIGURE 21. Detail of dynamic performance of proposed decoupled GFM controller (blue curves) and conventional VA-GFM (red curves) for different values of the virtual resistance R_v for SCR = 5. Solid curves: $R_v = 0.3$ pu; dashed curves: $R_v = 1$ p.u. Top: measured active power; bottom: measured reactive power.

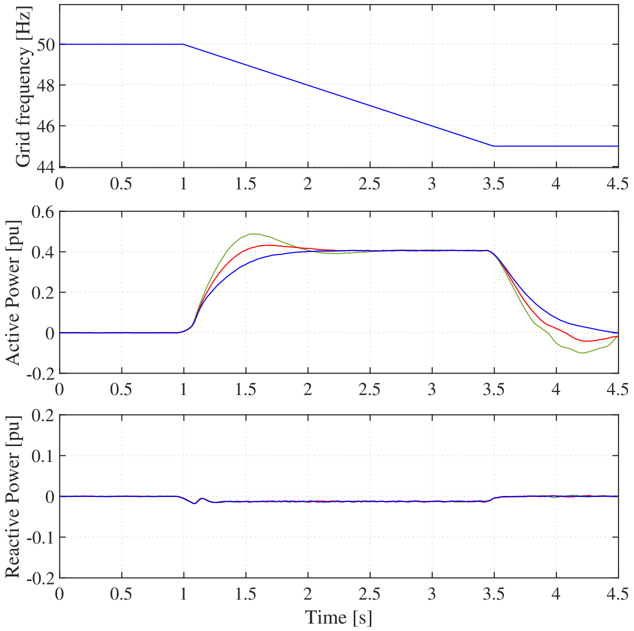

FIGURE 22. Dynamic performance of proposed decoupled GFM controller during RoCoF event for $\zeta_P = 0.5$ (green curves), $\zeta_P = 0.7$ (red curves), and $\zeta_P = 1$ (blue curves). Top: grid frequency; middle: measured active power; bottom: measured reactive power.

Finally, to validate the effectiveness of the proposed tuning mechanism for the APL and the ability to provide inertial power, an RoCoF event is applied to the system. In this study case, the frequency of the controllable-voltage source is reduced at a rate of 2 Hz/s from 50 to 45 Hz, while the active power reference is set to $P_{\text{ref}} = 0$ p.u. The loop bandwidth α_P is selected in accordance with (26) to achieve an inertia time constant $H = 5$ s. Consequently, for the applied frequency disturbance the inertial active-power response is 0.4 p.u. The loop bandwidth α_Q is kept as in Table 2. Fig. 22 illustrates the active power response of the converter for three different values of the damping ratio ζ_P. As observed, all cases produce the desired steady-state inertial-power. As expected, a lower damping ratio results in a faster rise time of the inertial power; its selection, depends on the system requirements.

VI. CONCLUSION

In this article, a novel control strategy for VA-GFM for effective decoupling between the active- and reactive-power responses has been presented. The proposed Decoupled VA-GFM controller is based on a complex-power outer control loop and employs a VA-compensation algorithm to achieve near-perfect decoupling between active and reactive power for any selection of the VA parameters. As a consequence, the virtual resistance in the VA can be selected arbitrary, depending on the system needs for damping in the subsynchronous-frequency range and at SFR.

This article also presents a detailed frequency analysis of the proposed controller. This analysis demonstrates that the different degrees of freedom in the controller can be used to influence the behavior in different frequency ranges independently. Furthermore, it is shown that for equal selection of the APL and RPL bandwidths, both the closed-loop transfer function and the converter's input admittance can be expressed as a single-dimensional transfer function, thus allowing for single-input/single-output representation of the decoupled VA-GFM. The effectiveness of the proposed approach over the conventional GFM control strategies are also verified through experimental tests.

APPENDIX

Consider a virtual admittance model where its resistive part is negligible: $Y_\text{v}(\omega) \approx 1/j\omega L_\text{v} \rightarrow \varphi_\text{Y}(\omega) = -\pi/2$. Using the circuit in Fig. 4, the virtual back-EMF voltage $\underline{v}_\text{EMF}$ can be derived from Figs. 7 and 8 as

$$\begin{aligned}\underline{v}_\text{EMF} &= e^{\underline{\xi}_\text{X} + j\theta_\text{N}} = e^{\underline{\xi}_\text{X}} e^{j\theta_\text{N}}\\ &= e^{|\gamma_\text{X} + j\varepsilon_\text{X}| e^{-j[\arg(\gamma_\text{X} + j\varepsilon_\text{X}) - \pi/2]}} e^{j\theta_\text{N}}\\ &= e^{|\gamma_\text{X} + j\varepsilon_\text{X}| e^{-j\arg(\gamma_\text{X} + j\varepsilon_\text{X})} e^{j\pi/2}} e^{j\theta_\text{N}}\\ &= e^{(\gamma_\text{X} - j\varepsilon_\text{X}) e^{j\pi/2}} e^{j\theta_\text{N}}\\ &= e^{(\varepsilon_\text{X} + j\gamma_\text{X})} e^{j\theta_\text{N}} = e^{\varepsilon_\text{X}} e^{j(\gamma_\text{X} + \theta_\text{N})}\\ &= V_{\text{EMF,X}} e^{j(\gamma_\text{X} + \theta_\text{N})}\end{aligned} \tag{30}$$

where the subscript "X" denotes that the controller outputs have been calculated considering a reactive input-admittance model. From the equations above, the voltage $\underline{v}_\text{EMF}$ has the same structure as for a conventional GFM control, with the APL and RPL deciding the voltage phase and magnitude through the corresponding output signals γ_X and ε_X, respectively. Note that the conventional controller generates the voltage magnitude, V, directly from the RPL, whereas in the proposed strategy the RPL's output is its natural logarithm (i.e., $\varepsilon = \ln(V)$), to guarantee the same control structure for APL and RPL.

The result in (30) also agrees with the power-flow equations derived from (2) and (3) for a purely reactive impedance ($Z_\text{v} = 1/Y_\text{v}$)

$$\begin{aligned}P_\text{g} &= \frac{V_\text{g} V_{\text{EMF,X}} \sin\delta}{Z_\text{v}} = \frac{V_\text{g} e^{\varepsilon_\text{X}} \sin\gamma_\text{X}}{Z_\text{v}}\\ Q_\text{g} &= \frac{V_\text{g} V_{\text{EMF,X}} \cos\delta - V_\text{g}^2}{Z_\text{v}} = \frac{V_\text{g} e^{\varepsilon_\text{X}} \cos\gamma_\text{X} - V_\text{g}^2}{Z_\text{v}}.\end{aligned} \tag{31}$$

Similarly, consider now the extreme case of a virtual admittance model where the resistive part is dominant: $Y_\text{v}(\omega) \approx 1/R_\text{v} \rightarrow \varphi_\text{Y}(\omega) = 0$. The virtual voltage $\underline{v}_\text{EMF}$ can now be calculated as

$$\begin{aligned}\underline{v}_\text{EMF} &= e^{\underline{\xi}_\text{R} + j\theta_\text{N}} = e^{\underline{\xi}_\text{R}} e^{j\theta_\text{N}} = e^{|\gamma_\text{R} + j\varepsilon_\text{R}| e^{-j[\arg(\gamma_\text{R} + j\varepsilon_\text{R})]}} e^{j\theta_\text{N}}\\ &= e^{(\gamma_\text{R} - j\varepsilon_\text{R})} e^{j\theta_\text{N}} = e^{\gamma_\text{R}} e^{j(-\varepsilon_\text{R} + \theta_\text{N})}\\ &= V_{\text{EMF,R}} e^{j(-\varepsilon_\text{R} + \theta_\text{N})}\end{aligned} \tag{32}$$

where the subscript "R" denotes that the controller outputs have been calculated considering a resistive input-admittance model. As can be observed, the role of the active- and reactive-power controllers to generate the phase and magnitude of $\underline{v}_\text{EMF}$ is reversed as compared with the reactive impedance case: $|\underline{v}_\text{EMF}|$ controls the active power, while $\angle(\underline{v}_\text{EMF})$ controls reactive power. This is inline with the power-flow equations derived from (2) and (3) for a purely resistive impedance

$$\begin{aligned}P_\text{g} &= \frac{V_\text{g} V_{\text{EMF,R}} \cos\delta - V_\text{g}^2}{Z_\text{v}} = \frac{V_\text{g} e^{\gamma_\text{R}} \cos\varepsilon_\text{R} - V_\text{g}^2}{Z_\text{v}}\\ Q_\text{g} &= \frac{-V_\text{g} V_{\text{EMF,R}} \sin\delta}{Z_\text{v}} = \frac{-V_\text{g} e^{\gamma_\text{R}} \sin\varepsilon_\text{R}}{Z_\text{v}}.\end{aligned} \tag{33}$$

While the conventional VA-GFM would have generated the phase and magnitude of $\underline{v}_\text{EMF}$ in a similar form as in (30), regardless of the selected parameters for the virtual admittance (leading to a deteriorated dynamic performance with nonnegligible R_v), thanks to the implemented phase compensation the role of the controller outputs γ and ε adapts automatically in the decoupled GMF. For the two extreme cases considered in this appendix, moving from a reactive to a resistive model of Y_v, leads to

$$\begin{aligned}\varepsilon_\text{X} &\rightarrow \gamma_\text{R}\\ \gamma_\text{X} &\rightarrow -\varepsilon_\text{R}\end{aligned}$$

yielding to the same active- and reactive-power flow in (31) and (33).

REFERENCES

[1] International Energy Agency, "Net zero by 2050: A roadmap for the global energy sector," May 2021. [Online]. Available: https://www.iea.org/reports/net-zero-by-2050

[2] B. K. Bose, "Global energy scenario and impact of power electronics in 21st century," *IEEE Trans. Ind. Electron.*, vol. 60, no. 7, pp. 2638–2651, 2013. [Online]. Available: https://ieeexplore.ieee.org/abstract/document/6214597

[3] ENTSO-E, "High penetration of power electronic interfaced power sources and the potential contribution of grid forming converters," n.d. [Online]. Available: https://eepublicdownloads.entsoe.eu/clean-documents/Publications/SOC/High_Penetration_of_Power_Electronic_Interfaced_Power_Sources_and_the_Potential_Contribution_of_Grid_Forming_Converters.pdf

[4] J. Matevosyan et al., "Grid-forming inverters: Are they the key for high renewable penetration," *IEEE Power Energy Mag.*, vol. 17, no. 6, pp. 89–98, Nov./Dec. 2019.

[5] R. Rosso, X. Wang, M. Liserre, X. Lu, and S. Engelken, "Grid-forming converters: Control approaches, grid-synchronization, and future trends — A review," IEEE Open J. Ind. Appl., vol. 2, pp. 93–109, 2021. [Online]. Available: https://ieeexplore.ieee.org/document/9408354/

[6] S. D'Arco and J. A. Suul, "Virtual synchronous machines — Classification of implementations and analysis of equivalence to droop controllers for microgrids," in *Proc. IEEE Grenoble Conf.*, 2013, pp. 1–7.

[7] M. Tozak, S. Taskin, I. Sengor, and B. P. Hayes, "Modeling and control of grid forming converters: A systematic review," *IEEE Access*, vol. 12, pp. 107818–107843, 2024. [Online]. Available: https://ieeexplore.ieee.org/abstract/document/10620991

[8] L. Zhang, L. Harnefors, and H. Nee, "Power-synchronization control of grid-connected voltage-source converters," IEEE Trans. Power Syst., vol. 25, no. 2, pp. 809–820, May 2010.

[9] P. Rodriguez, I. Candela, C. Citro, J. Rocabert, and A. Luna, "Control of grid-connected power converters based on a virtual admittance control loop," in *Proc. 15th Eur. Conf. Power Electron. Appl.*, 2023, pp. 1–10.

[10] M. Li et al., “Unified modeling and analysis of dynamic power coupling for grid-forming converters,” *IEEE Trans. Power Electron.*, vol. 37, no. 2, pp. 2321–2337, Feb. 2022. [Online]. Available: https://ieeexplore.ieee.org/document/9521708

[11] Z. Tang, S. Wang, Y. Cui, X. Cheng, and Y. Zhao, “A review of coupling and interaction studies of grid-forming converters based on transient stability,” in *Proc. 7th Int. Conf. Energy, Elect. Power Eng.*, 2024, pp. 259–265. [Online]. Available: https://ieeexplore.ieee.org/abstract/document/10586409

[12] F. Zhao, X. Wang, and T. Zhu, “Low-frequency passivity-based analysis and damping of power-synchronization controlled grid-forming inverter,” *IEEE J. IEEE Trans. Emerg. Sel. Topics Power Electron.*, vol. 11, no. 2, pp. 1542–1554, Apr. 2023. [Online]. Available: https://ieeexplore.ieee.org/document/9934914

[13] K. Kamalinejad, A. Narula, M. Bongiorno, M. Beza, and J. R. Svensson, “Investigation of control parameters’ impact on damping property of grid-forming converters,” in *Proc. IEEE Energy Convers. Congr. Expo.*, 2024, pp. 686–693. [Online]. Available: https://ieeexplore.ieee.org/document/10860863

[14] C. R. Shah, M. Molinas, R. Nilsen, and M. Amin, “Impedance reshaping of GFM converters with selective resistive behaviour for small-signal stability enhancement,” in *Proc. IEEE Appl. Power Electron. Conf. Expo.*, 2024, pp. 1619–1626, [Online]. Available: https://ieeexplore.ieee.org/document/10509416

[15] P. Zhang, H. Zhao, H. Cai, J. Shi, and X. He, “Power decoupling strategy based on ‘virtual negative resistor’ for inverters in low-voltage microgrids,” *IET power electron.*, vol. 9, no. 5, pp. 1037–1044, Apr. 2016. [Online]. Available: https://onlinelibrary.wiley.com/doi/abs/10.1049/iet-pel.2015.0137

[16] K. D. Brabandere, B. Bolsens, J. V. D. Keybus, A. Woyte, J. Driesen, and R. Belmans, “A voltage and frequency droop control method for parallel inverters,” IEEE Trans. Power Electron., vol. 22, no. 4, pp. 1107–1115, Jul. 2007. [Online]. Available: https://ieeexplore.ieee.org/document/4267747

[17] T. Wu, Z. Liu, J. Liu, S. Wang, and Z. You, “A unified virtual power decoupling method for droop-controlled parallel inverters in microgrids,” *IEEE Trans. Power Electron.*, vol. 31, no. 8, pp. 5587–5603, Aug. 2016, [Online]. Available: https://ieeexplore.ieee.org/abstract/document/7317801/figures#figures

[18] B. Li and L. Zhou, “Power decoupling method based on the diagonal compensating matrix for VSG-controlled parallel inverters in the microgrid,” Energies, vol. 10, no. 12, 2017, Art. no. 2159. [Online]. Available: https://www.mdpi.com/1996-1073/10/12/2159

[19] Y. Tao et al., “Power decoupling control of grid-forming converter based on voltage and angle compensation,” in *Proc. 6th Int. Conf. Elect. Eng. Green Energy*, 2023, pp. 95–100. [Online]. Available: https://ieeexplore.ieee.org/document/10246724/referencesreferences

[20] P. Wang, M. Chen, J. Wang, G. Zhu, and F. Jiang, “An active power feedforward compensation-based power decoupling method for droop control converters,” *IEEE Trans. Power Electron.*, vol. 40, no. 5, pp. 6726–6739, May 2025, [Online]. Available: https://ieeexplore.ieee.org/document/10849952

[21] P. Imgart, M. Beza, M. Bongiorno, and J. R. Svensson, “An overview of grid-connection requirements for converters and their impact on grid-forming control,” in *Proc. 24th Eur. Conf. Power Electron. Appl.*, 2022, pp. 1–10.

[22] Nature. Energy System Operator, “The grid code,” 2024, [Online]. Available: https://dcm.nationalenergyso.com/

[23] A. Narula, M. Bongiorno, and M. Beza, “Comparison of grid-forming converter control strategies,” in *Proc. IEEE Energy Convers. Congr. Expo.*, 2021, pp. 361–368.

[24] L. Harnefors, M. Hinkkanen, U. Riaz, F. M. M. Rahman, and L. Zhang, “Robust analytic design of power-synchronization control,” *IEEE Trans. Ind. Electron.*, vol. 66, no. 8, pp. 5810–5819, Aug. 2019.

[25] M. G. Taul, X. Wang, P. Davari, and F. Blaabjerg, “Current limiting control with enhanced dynamics of grid-forming converters during fault conditions,” *IEEE Trans. Emerg. Sel. Topics Power Electron.*, vol. 8, no. 2, pp. 1062–1073, Jun. 2020. [Online]. Available: https://ieeexplore.ieee.org/document/8779657/

[26] F. Zhao, T. Zhu, Z. Li, and X. Wang, “Low-frequency resonances in grid-forming converters: Causes and damping control,” *IEEE Trans. Power Electron.*, vol. 39, no. 11, pp. 14430–14447, Nov. 2024.

[27] P. Imgart, A. Narula, M. Bongiorno, M. Beza, and J. R. Svensson, “A cascaded power controller for robust frequency ride-through of grid-forming converters,” in *Proc. IEEE Energy Convers. Congr. Expo.*, 2022, pp. 1–8.

[28] P. Imgart, A. Narula, M. Bongiorno, M. Beza, and J. R. Svensson, “External inertia emulation to facilitate active-power limitation in grid-forming converters,” *IEEE Trans. Ind. Appl.*, vol. 60, no. 6, pp. 9145–9156, Nov./Dec. 2024. [Online]. Available: https://ieeexplore.ieee.org/document/10637739/?arnumber=10637739

[29] M. Beza and M. Bongiorno, “On the risk for subsynchronous control interaction in Type 4 based wind farms,” *IEEE Trans. Sustain. Energy*, vol. 10, no. 3, pp. 1410–1418, Jul. 2019.

PAUL IMGART (Member, IEEE) received the B.Sc. and M.Sc. degrees in power engineering from Leibniz University Hannover, Germany, in 2015 and 2017, respectively, and the Ph.D. degree in electric power engineering from the Chalmers University of Technology, Göteborg, Sweden, in 2025.

His research interest includes the stability and robustness of sustainable power grids, with particular focus on innovative converter control strategies for converter-dominated systems.

ANANT NARULA (Member, IEEE) received the joint M.Sc. degree in smart electrical networks and systems (EIT InnoEnergy) from the KTH Royal Institute of Technology, Stockholm, Sweden, and the Universitat Politècnica de Catalunya, Barcelona, Spain, in 2018, and the Ph.D. degree in electric power engineering from the Chalmers University of Technology, Göteborg, Sweden, in 2023.

He is currently a Research Specialist with the Chalmers University of Technology. His research interests include the applications of power electronics in power systems, converter control, and stability studies of power systems.

MASSIMO BONGIORNO (Senior Member, IEEE) received the M.Sc. degree in electrical engineering from the University of Palermo, Palermo, Italy, in 2002, and the Lic. Eng. and Ph.D. degrees in electric power engineering from the Chalmers University of Technology, Gothenburg, Sweden, in 2004 and 2007, respectively.

From 2007 to 2010, he was an Assistant Professor with the Department of Electric Power Engineering, Chalmers University of Technology, where he became an Associate Professor in 2010. Since 2015, he has been a Professor in power electronic applications for power systems, and since 2020 he is the Head of the Division of Electric Power Engineering, Chalmers University of Technology. Since 2022, he has been the Director of the centre of excellence The Swedish Electricity Storage and Balancing Centre, Chalmers University of Technology. His research interests include the application of power electronics in power systems, converter control, power system dynamics, and power quality.

MEBTU BEZA (Member, IEEE) received the B.Sc. degree in electrical engineering from Bahir Dar University, Bahir Dar, Ethiopia, in July 2005, and the M.Sc., Lic.Eng., and Ph.D. degrees in electric power engineering from the Chalmers University of Technology, Gothenburg, Sweden, in 2009, 2012, and 2015, respectively, and the D.Sc. degree (Docent) in control and modeling of power electronic converters in power systems from the Chalmers University of Technology, in 2020.

He is currently an Associate Professor with the Chalmers University of Technology. His research interests include signal processing in power systems, control theory, stability studies in converter-dominated systems, converter topologies and application of power electronics in power systems.

JAN R. SVENSSON (Senior Member, IEEE) received the Ph.D. and D.Sc. degrees (Docent) in electric power engineering from the Chalmers University of Technology, Göteborg, Sweden, in 1988 and 2002 respectively.

From 1999 to 2009, he was with ABB in R&D of HVDC Transmission, STATCOMs, and energy storages, especially design and control of light-concept devices (HVDC and FACTS). Between 2009 and 2014, he was the Program Manager for the Global R&D Program "Active Grid Infrastructure" with ABB Corporate Research. From 2014 to 2020, he was a Senior Principal Scientist on power electronics systems with ABB Power Grids Research. In addition to his current role as a Research Fellow with Hitachi Energy Research, Västerås, Sweden, he has also been an Adjunct Professor with the Chalmers University of Technology since 2018. His research interests include design and control of power electronics in power systems, power quality, storage technologies, and renewable energy.

JEAN-PHILIPPE HASLER received the M.Sc. degree in electrical engineering from the Ecole Polytechnique Fédérale de Lausanne, Lausanne, Switzerland, in 1986.

In 1986, he joined BBC where he was developing control systems and protection algorithms for multiterminal HVDC. Since 1993, he has been with ABB, conducting power system and control studies for different FACTS applications. Since 2014, he has been with ABB, where he is currently a Senior Principal Engineer with Hitachi Energy, Västerås, Sweden.

PAOLO MATTAVELLI (Fellow, IEEE) received the M.S. (Hons.) and Ph.D. degrees in electrical engineering from the University of Padova, Padova, Italy, in 1992 and 1995, respectively.

He is currently a Full Professor in electronics with the University of Padova. His current Google scholar H-index is 90. His research interests include analysis, modeling, and control of power converters, grid-connected converters for renewable energy systems and microgrids, and high-temperature and high-power-density power electronics.

Dr. Mattavelli was the recipient of the Prize Paper Award in IEEE TRANSACTIONS ON POWER ELECTRONICSin 2005, 2006, 2011, and 2012, and the second Prize Paper Award at the IEEE Industry Applications Society Annual Meeting in 2007. From 2003 to 2012, he was an Associate Editor for IEEE TRANSACTIONS ON POWER ELECTRONICS. From 2003 to 2006, 2006 to 2009, and 2013 to 2015, he was a Member-At-Large of the IEEE Power Electronics Society's Administrative Committee. From 2005 to 2010, he was the Industrial Power Converter Committee Technical Review Chair for IEEE TRANSACTIONS ON INDUSTRY APPLICATIONS. From 2018 to 2024, he was a Co-Editor-in-Chief for IEEE TRANSACTIONS ON POWER ELECTRONICS.